chemistry

MDPI

Article

Tailoring the Photothermal Properties of Iron-Based MOFs via Tannic Acid-Enabled Post-Synthetic Modification

Farnaz Shammiry and Alejandro Montesinos-Castellanos *

Tecnologico de Monterrey, Artificial Intelligence for Manufacturing and Supply Chain Institute, Ave. Eugenio Garza Sada 2501 Sur, Col. Tecnológico, Monterrey 64700, Nuevo León, Mexico; a00835355@tec.mx
* Correspondence: alejandro_montesinos@tec.mx

Abstract

Harvesting solar energy and its direct conversion into heat via a photothermal strategy represent a clean and sustainable pathway for green thermal energy generation. However, achieving high photothermal conversion efficiency requires materials with broad optical absorption, structural robustness, and long-term cycling stability. Although Metal–Organic Frameworks (MOFs) have shown promising results across various fields due to their highly tunable architectures, unmodified MOFs frequently suffer from poor visible-light harvesting and low photothermal efficiency. In this study, MIL-53(Fe) and MOF-235(Fe) were selected, and their structural dynamics were tuned by post-synthetic modification (PSM) with tannic acid (TA) in order to engineer their visible-light photothermal performance. MOF-235(Fe) and PVP-modulated MIL-53(Fe) were synthesized via a rapid sonochemical route and modified with varying tannic acid loadings. Following post-synthetic modification, the sonochemically synthesized PVP-modulated MIL-53(Fe) preserved its framework topology, enabling MIL-53/TA150 to achieve an exceptional photothermal response that reached ≈47 °C under visible laser irradiation (632.5 nm). However, the inherent hydrolytic instability of MOF-235 conventionally poses a major limitation for classical post-synthetic modification and photothermal evaluation. Herein, a one-pot water-induced dissolution–construction process was employed during the tannic acid modification of sonochemically synthesized MOF-235, wherein localized leached Fe^{3+} ions in aqueous media promoted the in situ self-assembly of photothermally active metal–phenolic networks (MPNs), which consequently induced visible-light photothermal performance and elevated the surface temperature of MOF-235/TA150 to ≈37 °C. Overall, this work demonstrated that surface engineering and tailoring the structural dynamics of MOFs provide a powerful strategy for developing visible-light-responsive MOFs for green thermal energy generation.

Keywords: Metal–Organic Frameworks (MOFs); post-synthetic modification; photothermal; visible-light-to-heat; tannic acid

Check for updates

Academic Editor: Miguel Jose Yacaman

Received: 23 October 2026
Revised: 6 November 2026
Accepted: 10 November 2026
Published: 23 November 2026

Copyright: © 2026 by the authors. Licensee MDPI, Basel, Switzerland. This article is an open access article distributed under the terms and conditions of the Creative Commons Attribution (CC BY) license.

1. Introduction

Population growth and industrialization have contributed to an increase in global energy demand, particularly for thermal energy, which accounts for nearly half of global final energy consumption. However, heat generation still relies heavily on fossil fuels, which are a major source of greenhouse gas emissions and contribute to air pollution, posing serious threats to human health worldwide [1–4]. According to the World Health Organization (WHO), air pollution was responsible for an estimated 4.2 million premature deaths in 2019 [5]. Consequently, there is a critical need to develop sustainable approaches

for heat generation that reduce dependence on fossil-fuel-based energy sources and utilize renewable energy, particularly solar energy [6].

While various strategies and technologies have been developed to harness solar energy and convert it into useful thermal energy, photothermal conversion has attracted considerable attention because of its ability to efficiently convert absorbed visible light energy into thermal energy [7]. This process relies on photothermal materials, which have emerged as promising candidates for a wide range of applications, including seawater desalination and purification, greenhouse gas conversion and desorption, photothermal catalysis, energy storage and conversion, sensing, and biomedical applications such as phototherapy, drug delivery, and medical devices. Various organic and inorganic materials, such as carbon nanotubes, noble metals, and polymers, have been investigated and modified to achieve efficient light-to-heat conversion [8,9]. Although these materials have demonstrated promising photothermal performance, some may exhibit limitations such as low structural tunability, limited long-term stability and poor environmental resistance; consequently, they may fail to achieve high photothermal efficiency [10]. For instance, limited resistance to the environment, such as humidity, can affect their long-term performance, whereas the relatively high cost of some photothermal materials may hinder their economic viability and large-scale commercialization [11,12]. These limitations have motivated researchers to explore alternative materials capable of addressing these challenges.

Among emerging functional materials, Metal–Organic Frameworks (MOFs), constructed from organic (ligand) and inorganic (metal cluster) components, have attracted considerable attention due to their special physicochemical properties such as crystalline nature, well-defined porosity, and highly tunable structures, which make them great candidates for various applications including gas storage, separation, electronic devices and catalysis [13,14]. In particular, tailorable metal-ligand coordination provides opportunities to adjust and enhance their optical properties for photophysical/chemical applications [15,16]. MOFs consist of continuous chains of transition-metal nodes bridged by organic linkers, resembling 1D inorganic semiconductors [17]. Photothermal processes occur in such semiconductor structures when photogenerated charge carriers undergo non-radiative relaxation pathways that generate thermal energy [18]. Therefore, the metal-ligand chain in MOFs can induce strong ligand-to-metal charge transfer (LMCT), increasing light harvesting and resulting in non-radiative relaxation mechanisms into thermal energy [19].

Recent studies have demonstrated the potential of MOFs as photothermal materials [20,21]. For example, Ji et al. reported enhanced photothermal performance for a core–shell PCN-224@ZIF-8 heterojunction MOF, where visible-light irradiation increased the local temperature to ≈54 °C for a biomedical application [22]. In another study, Espin et al. demonstrated that direct irradiation of MOFs using a UV–Vis light source induced localized light-to-heat conversion, which facilitated thermal activation and reduced the time required for solvent-exchange procedures or even vacuum conditions compared with conventional approaches [23]. These studies demonstrated that MOFs can function not only as porous frameworks but also as tuneable materials for light-to-heat conversion. Despite the promising progress achieved with MOFs as photothermal materials, their practical implementation remains challenged by synthesis cost, energy consumption, scalability, and the use of expensive or non-sustainable precursors. Several strategies such as using low-cost precursors, greener synthesis approaches, and rational modification of MOFs have therefore been explored and mentioned in the literature to improve their practical feasibility [16,24,25].

Among the different types of MOFs, Fe-based MOFs are particularly attractive due to their Fe oxo-cluster in various fields, particularly in photophysical/chemical applications. Iron as a metal core in Fe-MOFs offers notable benefits, including natural abundance,

cost-effectiveness, and low toxicity compared to other transition metals. Furthermore, one-dimensional Fe-O linkages can enhance visible-light harvesting, which makes it a promising candidate for light-driven applications [26,27]. Although Fe-based MOFs span various topologies, including MIL-100(Fe), MIL-101(Fe), MIL-53(Fe), and MOF-235(Fe), only a few have received significant research attention for photothermal applications [28,29]. For instance, Dong et al. reported a photothermal conversion efficiency of ≈21% for MIL-101(Fe) nanoparticles coated with Cu-TA [30].

Although MOF-235(Fe) and MIL-53(Fe) possess distinct structural characteristics, their photothermal properties under visible-light irradiation have received insufficient attention. Both MOFs act as n-type semiconductors, which have shown promising photoactivity under visible-light irradiation [17,31]. In particular, MOF-235 forms a relatively rigid porous framework containing coordinatively unsaturated iron sites and functional organic linkers [32]. This structure provides multiple interaction sites and redox activity, enabling applications in electrochemical sensing, magnetism-related technologies, gas storage, pollutant adsorption and photocatalysis under visible light irradiation [31,33–35]. In contrast, MIL-53(Fe) has demonstrated exceptional characteristics such as pore flexibility and a thermodynamically stable framework. The flexible pore structure of MIL-53, known as "breathing" behavior, influences its optical properties and, consequently, its photocatalytic and photothermal behavior [36,37]. Ling et al. reported that breathing transitions in MOFs can exert a major influence on the bandgap (Eg); for instance, the dehydrated narrow pore (np) form of MIL-53(Fe) (unit cell volume = 832.9 $Å^3$) showed Eg = 2.70 eV, whereas the hydrated form (unit cell volume = 973.1 $Å^3$) exhibited Eg = 3.41 eV [38].

Despite the attractive characteristics of MOF-235(Fe) and MIL-53(Fe), they have been studied mostly for photocatalytic applications. Moreover, some limitations such as the low hydrolytic stability of MOF-235 and the predominant near-infrared (NIR) photothermal responsiveness of MIL-53 have limited their direct photothermal application under the visible solar spectrum. Therefore, it is necessary to tailor their surface chemistry, improve framework stability, and enhance their visible-light photothermal performance.

According to the literature, functionalization of MOFs could improve visible light absorption and its conversion into thermal energy [20,36,39]. Adjusting the physical and chemical properties through the incorporation of additional functional groups represents an effective strategy to induce photothermal properties and enhance material performance [40]. Post-Synthetic Modification (PSM) provides a facile and effective strategy after synthesis for tuning the internal porosity and external surface characteristics of MOFs. Through PSM, additional functional groups or molecular species can be introduced to the MOF particles without necessarily altering the framework structure, thereby providing opportunities to modify surface chemistry, adsorption behavior, stability, and other functional properties [39,41]. In particular, the incorporation of functional groups capable of interacting with metal centers or organic linkers can alter the physicochemical environment of the framework and potentially influence its interaction with light [42]. Although various materials, including acids, bases, and polymers, have been employed for the surface modification of MOFs, several challenges remain. For instance, amine-containing functionalities have been widely investigated for modifying the properties of MOFs; however, hydroxyl-rich functionalities can provide additional advantages, including strong hydrogen-bonding capability, favorable interactions with metal centers, and potentially improved chemical and environmental stability [43]. Moreover, hydroxyl-containing materials (–OH) are inherently amphoteric, which allows them to act as either proton donors or proton acceptors depending on the environment [44].

Hydrolysable tannins, particularly Tannic Acid (TA), are polyphenolic compounds rich in hydroxyl functional groups. Despite the amphoteric nature of tannic acid, its chemical

structure contains abundant phenolic hydroxyl (–OH) and carbonyl (C=O) groups attached to aromatic rings, providing multiple interaction pathways, including hydrogen bonding, electrostatic interactions, π–π interactions and most importantly, metal coordination [45,46]. TA exhibits strong chelating ability toward metal ions through Lewis acid–base interactions, enabling coordination with unsaturated Fe sites in iron-based MOFs [47]. Through such interactions, TA serves as a versatile framework-modification agent, which provides multifunctional enhancements to the physicochemical properties of MOFs. For instance, the interaction of TA with the unsaturated Fe sites of the MOF generates numerous Fe-O complexes, belonging to iron–polyphenol networks, that enhance charge-transfer transitions, particularly ligand-to-metal charge transfer (LMCT). This enhancement of LMCT can improve visible-light harvesting by facilitating photogenerated electron-hole creation and subsequent non-radiative relaxation into thermal energy [48]. Furthermore, the presence of abundant phenolic hydroxyl groups has been reported to enhance structural stability, while introducing additional active sites for adsorption and guest interactions [49–51]. Therefore, TA could be a promising candidate for the post-synthetic modification (PSM) of Fe-based MOFs to tailor their photothermal properties under visible light irradiation [19,52].

Tannic acid has previously been reported as a PSM agent for MIL-53(Fe) in photothermal applications [53]. However, previous studies relied on a single amount of TA (e.g., a 1:1 mass ratio of MOF to TA) under near-infrared (NIR) excitation, without systematically evaluating how TA loading governs intrinsic photothermal properties, particularly under visible-light irradiation. Furthermore, the interaction between TA and Fe-based MOFs depends strongly on the conditions under which the MOFs were synthesized. The synthetic route, along with additives and modulators used during framework growth, strongly influences surface chemistry, particle morphology, textural porosity, and the availability of active coordination sites. Whereas previous studies relied mostly on conventionally (solvothermally) synthesized MIL-53(Fe), alternative synthetic routes, such as sonochemical synthesis, yield frameworks with distinct surface characteristics that can alter subsequent post-synthetic reactivity.

In our previous work, we established a rapid sonochemical synthesis of MOF-235 (6 h at 70 °C) and demonstrated that PVP modulation drives a controlled structural phase transformation from MOF-235 to the thermodynamically stable MIL-53(Fe) phase [54]. This synthesis condition for both Fe-MOFs may influence the interaction between TA and the MOF framework; consequently, it may affect the structural, chemical, textural, and photothermal properties of the PSM MOFs. Accordingly, to the best of our knowledge, tannic acid was employed for the first time as a PSM agent to tailor the physicochemical properties and visible-light photothermal performance of the sonochemically synthesized MOF-235(Fe) and PVP-modulated MIL-53(Fe). Two key research questions are addressed in this study: (i) how TA loading governs the structural, textural, and optical absorption properties of each framework; and (ii) whether the resulting composites convert visible (632.5 nm) light, rather than near-infrared light, into heat with cycling stability.

2. Materials and Methods

2.1. Materials

All the chemicals were used as purchased without any further purification. Terephthalic acid (H_2BDC, 98%), Iron chloride hexahydrate ($FeCl_3{\cdot}6H_2O$, ≥99%), N,N -Dimethylformamide (DMF, ≥99.8%), Polyvinylpyrrolidone K30 (PVP), Tannic acid ($C_{76}H_{52}O_{46}$) and Methanol (CH_3OH, 99.9%) were purchased from Sigma-Aldrich Company (Toluca, México).

2.2. Synthesis of MOF-235(Fe) and MIL-53(Fe)

MOF-235(Fe) and MIL-53(Fe) were synthesized following previously reported sonochemical methodologies corresponding to PVP-0/MM and PVP-2/MW, respectively [54].

For MOF-235(Fe) synthesis, terephthalic acid (12 mmol) and iron(III) chloride hexahydrate (12 mmol) were dissolved in 60 mL of DMF and stirred for 30 min. For MIL-53(Fe), terephthalic acid (12 mmol), iron(III) chloride hexahydrate (12 mmol) and Polyvinylpyrrolidone (PVP, 173 mmol) were dissolved in 60 mL of DMF and stirred for 30 min at room temperature. The obtained solutions were transferred to reactors equipped with an ultrasonic probe (VCX 750, Sonics & Materials, Inc. Newtown, CT, USA) and sonicated for 6 h at 33% power (20 kHz, 750 W maximum power output). The reaction temperature was maintained at 70 ± 2 °C using a circulating water bath. After the reaction time, the suspended solid was cooled to room temperature; the resulting MOF suspension was separated and washed three times via centrifugation at 13,000 rpm (25 °C). The final solids were dried at 160 °C for 15 h (1 atm under air) and denoted as MOF-235 and MIL-53.

2.3. Post-Synthetic Modification of MOFs with Tannic Acid (TA)

MOF/TA particles were prepared based on a previously reported strategy for tannic acid coordination onto MIL-53(Fe) [53]. First, 150 mg MOF (MOF-235 or MIL-53) was dispersed in 150 mL of deionized water and stirred for 15 min (solution I). Tannic Acid (TA) at specified loadings of 50, 100 and 150 mg was gradually added to solution I, followed by continuous stirring for 60 min to ensure complete interaction (total stirring time: 75 min, at ambient temperature ≈ 25 °C). The resulting suspension was washed two times with deionized water via centrifugation at 13,000 rpm (25 °C). The final solid was redispersed in deionized water using an ultrasonic bath, transferred to a beaker, and dried at 70 °C for 16 h under ambient air (1 atm). The resulting samples were labelled as MOF-235/TAx and MIL-53/TAx, where "x" represents the amount (mg) of TA used for modification. For comparative control experiments, 150 mg of MOF-235 or MIL-53 was dispersed in 150 mL deionized water and stirred for 75 min without TA, followed by identical washing and drying procedures. The water-treated samples were labelled MOF-235/TA0 and MIL-53/TA0.

2.4. Characterization

To investigate the physicochemical properties of the prepared samples, all characterizations in this work were performed on freshly prepared samples, immediately following their synthesis and PSM. X-ray diffraction (XRD) patterns were recorded on a PANalytical (X'Pert Pro PW1800, Malvern, UK) diffractometer using Cu Kα ($\lambda = 0.154$ nm). Fourier transform infrared spectroscopy was carried out by a PerkinElmer Frontier (México City, Mexico) spectrometer in the range of 400–4000 cm^{-1}. The nitrogen adsorption−desorption isotherm was obtained with a NOVA Touch LX1 at 77 K; in each case, the sample was vacuum-dried at 120 °C for 12 h before analysis. Ultraviolet–Visible–Near Infrared Diffuse Reflectance Spectra (UV–vis–NIR DRS) were recorded using an Agilent Cary 5000 UV/Vis–NIR spectrophotometer. Thermogravimetric analysis (TGA) was performed to identify the temperatures of thermal events; a Linseis TGA-PT1600 instrument was used for this purpose. The morphology of the materials was determined by scanning electron microscopy (Zeiss EVO MA25 microscope, Oberkochen, Germany). Raman spectroscopic measurements were carried out on a Horiba Xplora Plus (HORIBA Scientific, Palaiseau, France) employing a 532 nm excitation laser, with signal detection performed via a Synapse Plus CCD detector covering a spectral window of 200–1700 cm^{-1}, data was processed using the labSpec 6.7 software. Thermal images were recorded by a FLIR Thermal Camera.

2.5. Photothermal Conversion Measurement

To investigate the photothermal performance of MOFs, approximately 35 mg of the dried powdered sample was uniformly spread onto a quartz slide to form a thin (≈1–2 mm) homogeneous square layer (≈11 mm × 11 mm) at ambient temperature. The prepared sample was positioned at a fixed distance of 17 cm from the light guide using a 632.5 nm HeNe laser (nominal laser output: 15 mW), delivering an incident power of 12.1 mW at the sample position (17 cm), as verified directly with an optical power meter. To eliminate interference from stray ambient light and air currents, the laser and sample setup were enclosed in a black box. The samples were subjected to continuous visible light irradiation for 10 min (600 s). To confirm that the generated heat was strictly driven by the MOF powders rather than substrate absorption, a bare quartz slide was irradiated under identical experimental conditions as a baseline control. The real-time surface temperature evolution and spatial thermal profiles of the samples during the irradiation process were monitored and recorded with an IR thermal camera. For durability and response testing, the sample was continuously irradiated for 40 min, followed by three light-on/off cycles (1 min laser off/2 min laser on) to evaluate photothermal switching stability.

3. Results and Discussion

3.1. Morphological Evolution and Textural Properties

Scanning electron microscopy (SEM) was performed to investigate the effect of Post-Synthetic Modification (PSM) with Tannic acid (TA) on the morphology of sonochemically synthesized MIL-53 and MOF-235. For conciseness, Figure 1 shows SEM images of water-treated (TA0) and maximum TA-functionalized (TA150) samples of both MOF series. SEM images of the complete MOF series are provided in the Supplementary Materials (Figure S1).

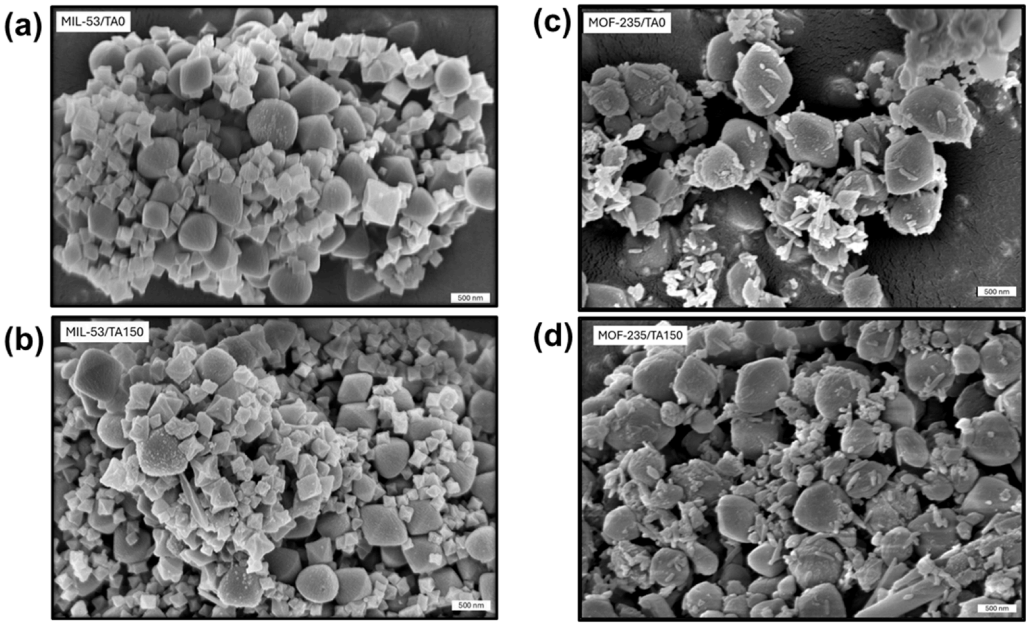

Figure 1. SEM images of water-treated (TA0) and PSM with the highest tannic acid loading (TA150): (**a**) MIL-53/TA0, (**b**) MIL-53/TA150, (**c**) MOF-235/TA0, and (**d**) MOF-235/TA150.

As shown in the SEM images of MIL-53/TA0 and MIL-53/TA150 (Figure 1a,b), particles maintained their characteristic hexagonal bipyramidal morphology, indicating that neither water dispersion nor PSM altered the overall MIL-53 particle morphology [55]. Conversely, noticeable morphological changes were observed in the SEM images of the

MOF-235 series (Figure 1c,d). While bipyramidal particles are observed in the SEM image of MOF-235, the SEM image of MOF-235/TA0 displays needle-like structures among the particles. These needle-shaped crystals were almost similar to unreacted species and/or partial decomposition products, as reported in our previous work [54]. The presence of these particles may suggest the hydrolytic instability and partial dissolution of the MOF-235 crystal under aqueous conditions while leaving behind the thermodynamically stable MIL-53 phase that co-formed during initial sonochemical synthesis. Following PSM of MOF-235 with different amounts of TA, no significant additional morphological changes were observed compared to the MOF-235/TA0 sample.

The textural properties of the MOFs were evaluated via nitrogen adsorption–desorption isotherms at 77 K. A comparison between MOFs before and after water treatment, and PSM with the highest amount of TA is illustrated in Figure 2. The complete series is given in Figure S2 and Table S1. According to the physisorption results of the MIL-53 series (Figure 2a), the textural parameters of MIL-53 before treatment agreed with values previously reported in our work [54]. However, MIL-53/TA0 exhibited a 23% reduction in surface area and a decrease in total pore volume compared to MIL-53. This behavior in MIL-53/TA0 could be due to improved purification and flexibility of the MIL-53 pores [56].

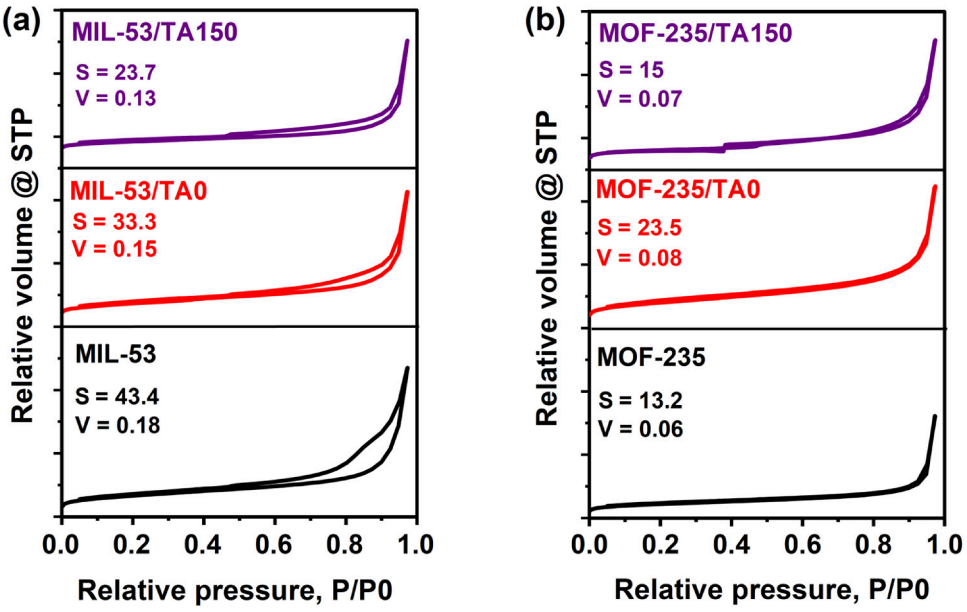

Figure 2. The nitrogen adsorption–desorption isotherms of (**a**) MIL-53 and (**b**) MOF-235, water-treated (TA0) and PSM with the highest tannic acid loading (TA150). S and V denote the surface area (m^2/g) and total pore volume (cm^3/g), respectively.

Following PSM of MIL-53 with TA, further reduction in surface area and total pore volume could be observed in the MIL-53/TA50, while the mathematically averaged pore diameter increased. This behavior may indicate TA molecules initially coat the surface of particles and selectively block or fill the small micropores, inaccessible to the nitrogen adsorbate molecules, as illustrated by the pore-size distribution in Figure S2 [45,57]. Interestingly, increasing the amount of TA in MIL-53/TA100 and MIL-53/TA150 resulted in a slight recovery of the textural properties. This trend could indicate that higher concentrations of TA provide the thermodynamic driving force required to overcome steric hindrance and force the polyphenol molecules deep into the pores rather than leaving them to accumulate on the surface of particles.

The physisorption results for the MOF-235 series are presented in Figures 2b and S2. The textural properties of MOF-235 were consistent with those reported in our previous

work. However, MOF-235/TA0 presented a higher surface area and total pore volume than MOF-235. This could be due to dissociation of $[FeCl_4]^-$ counter-anions through water treatment, while the thermodynamically stable MIL-53 phase, initially formed as part of a mixed Fe-MOF phase during our sonochemical synthesis, remained intact [54,58]. The textural properties of MOF-235/TA0 were close to those of MIL-53/TA0, further confirming the instability of MOF-235 in aqueous media. Following PSM of MOF-235 with TA, an initial increase in surface area and total pore volume was observed for MOF-235/TA50 compared to MOF-235/TA0, whereas a reverse trend occurred for MOF-235/TA100 and MOF-235/TA150. This may be attributable to anion exchange of water and/or TA interaction with the $[FeCl_4]^-$ species at nodal sites, along with TA interaction with the surviving MIL-53 framework.

3.2. Chemical and Crystalline Structure

To verify the morphological and textural observations, detailed spectroscopic (FTIR/Raman) and structural (XRD) characterizations were performed. The chemical bonding environments and functional groups of the MOFs were revealed by FTIR (Figure 3) and Raman spectroscopy (Figure 4).

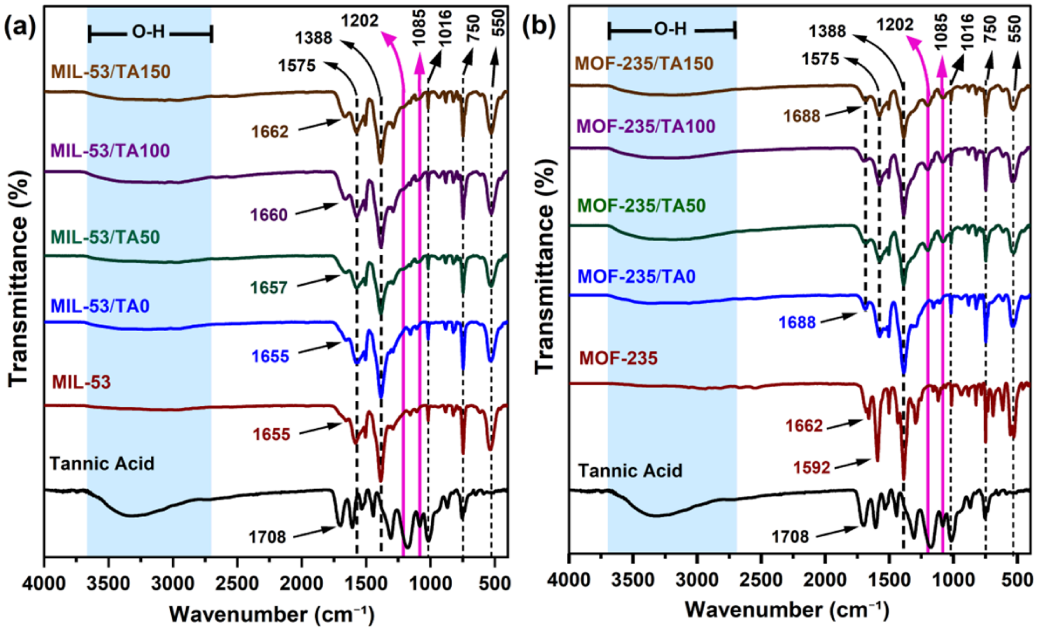

Figure 3. FTIR spectra of (**a**) MIL-53 and (**b**) MOF-235, water-treated and PSM with different amounts of tannic acid, compared with pristine tannic acid.

FTIR results of MIL-53 and MOF-235 series before and after PSM are shown in Figure 3. Across all the samples, key characteristic bands at 550, 750, and 1016 cm^{-1} were preserved. The band at 550 cm^{-1} is associated with the Fe–O chemical bonding, confirming the coordination between the iron centers and the oxygen atoms of the ligands. Additionally, the peaks at 750 and 1016 cm^{-1} correspond to the C-H vibrational modes of the benzene ring belonging to the ligand [54]. The retention of these characteristic bands in all the samples after PSM indicated that the incorporation of TA did not alter the main chemical bonding of the MOFs. This behavior can be attributed to several factors, such as the strong coordination between Fe centers and the BDC ligand of the MOF, where the moderately acidic pH of the solution during PSM (pH ≈ 3.5 during PSM) was insufficient to break or degrade the Fe–carboxylate bonds [54,59].

Regarding the MIL-53 series (Figure 3a), after PSM of MIL-53 with TA, two new weak peaks appeared at 1085 and 1202 cm^{-1} (indicated by pink arrows in Figure 3a), whereas the original peaks observed in MIL-53 and MIL-53/TA0 within this region almost disappeared. These changes may suggest the interaction between iron and ester groups of TA [47,52]. Furthermore, the symmetric ($\nu s(COO^-)$) and asymmetric ($\nu as(COO^-)$) stretching vibrations of coordinated carboxylate groups at 1388 and 1575 cm^{-1}, respectively, were preserved before and after PSM. However, following PSM with TA, the carboxyl stretching band exhibited a blue shift from 1655 cm^{-1} (in MIL-53 and MIL-53/TA0) to 1662 cm^{-1} (in MIL-53/TA150). This blue shift could be attributed to interactions between hydroxyl groups of TA and carboxyl groups of the BDC (ligand) and/or PVP (modulator) [53,60,61]. Additionally, increasing the amount of TA led to a slight enhancement of the broad band in the 2500–3600 cm^{-1} region, corresponding to O–H vibrations, which may belong to the phenolic groups of TA [62].

On the other hand, Figure 3b presents the FTIR spectra of the MOF-235 series. Although MOF-235 displayed characteristic peaks aligned with the literature, the water-treated sample (MOF-235/TA0) exhibited noticeable spectral alterations. While most of the main peaks belonging to terephthalic acid in MOF-235/TA0 remained the same, the asymmetric stretching band showed intensity reduction and a red shift from 1592 to 1575 cm^{-1}, making the FTIR spectra of MOF-235/TA0 closer to the MIL-53 pattern (red pattern belonging to MIL-53 in Figure 3a). Additionally, the carboxyl stretching band shifted from 1662 cm^{-1} in MOF-235 to 1688 cm^{-1} in MOF-235/TA0. This blue shift in the carboxyl stretching band in MOF-235/TA0 relative to MOF-235 can be attributed to the presence of the $[FeCl_4]^-$; anion in the structure of MOF-235, which makes this framework more susceptible to hydrolysis under aqueous environments [59]. Furthermore, as previously reported, 6 h ultrasound-assisted synthesis of Fe-MOFs can result in the formation of mixed Fe-MOF phases [54]. Therefore, dispersing MOF-235 particles in water resulted in the dissociation of $[FeCl_4]^-$ anion from the positive charge $[Fe_3O(C_8H_4O_4)_3(C_3H_7NO)_3]^+$ cluster and partial collapse of the MOF-235 framework, while the thermodynamically stable MIL-53 (formed during the sonochemical synthesis) remained intact. Moreover, the FTIR spectra of MOF-235 after PSM with TA showed trends almost similar to the PSM of the MIL-53 series. Following PSM of MOF-235, two bands at 1085 and 1202 cm^{-1} (indicated by pink arrows in Figure 3b) were observed, representing the TA−Fe complex [60]. Additionally, the slightly higher intensity of the O-H band (2500–3600 cm^{-1}) may indicate an increased number of OH groups from the phenolic group of tannic acid on the MOF-235 frameworks [62].

Raman spectroscopy provided complementary structural evidence supporting the FTIR findings. Raman spectra of the full MIL-53 and MOF-235 series before and after PSM are displayed in Figure 4. For the MIL-53 series (Figure 4a), the peaks at 630, 862, 1140, 1451, 1505 and 1610 cm^{-1} (indicated by green arrows in Figure 4a) are assigned to aromatic ring, C–H bending, and carboxylate vibrations of the BDC linker. Following PSM of MIL-53 with TA, peaks at 630, 862 and 1610 cm^{-1} were preserved, while new peaks emerged at 610, 1344, 1477 and 1570 cm^{-1} (indicated by pink arrows in Figure 4a). The band at 1570 cm^{-1} is attributed to the vibration of the benzene ring (8α) interacting with the metal [52]. The bands at 1344 and 1477 cm^{-1} confirmed the successful formation of the metal-TA complex [63]. Moreover, the band at 610 cm^{-1} was assigned to the Fe-O chelation [52].

On the other hand, Figure 4b displayed the characteristic Raman bands of sonochemically synthesized MOF-235, aligning with the literature reported for the conventional synthesis of MOF-235 [31]. A key diagnostic feature of MOF-235 was a well-defined band at 330 cm^{-1} (indicated by the grey arrow in Figure 4b), representing the stretching mode of the $[FeCl_4]^-$ counter-anion [31]. Remarkably, upon water treatment (MOF-235/TA0),

the peak at 330 cm^{-1} completely disappeared, and the Fe–O cluster vibration shifted from 454 to 480 cm^{-1}. This spectral evolution, which changed the Raman spectrum of MOF-235/TA0 to be nearly identical to that of MIL-53, provided direct evidence of water-induced counter-anion leaching and partial framework hydrolysis of the MOF-235 component, while the stable MIL-53 structure persisted.

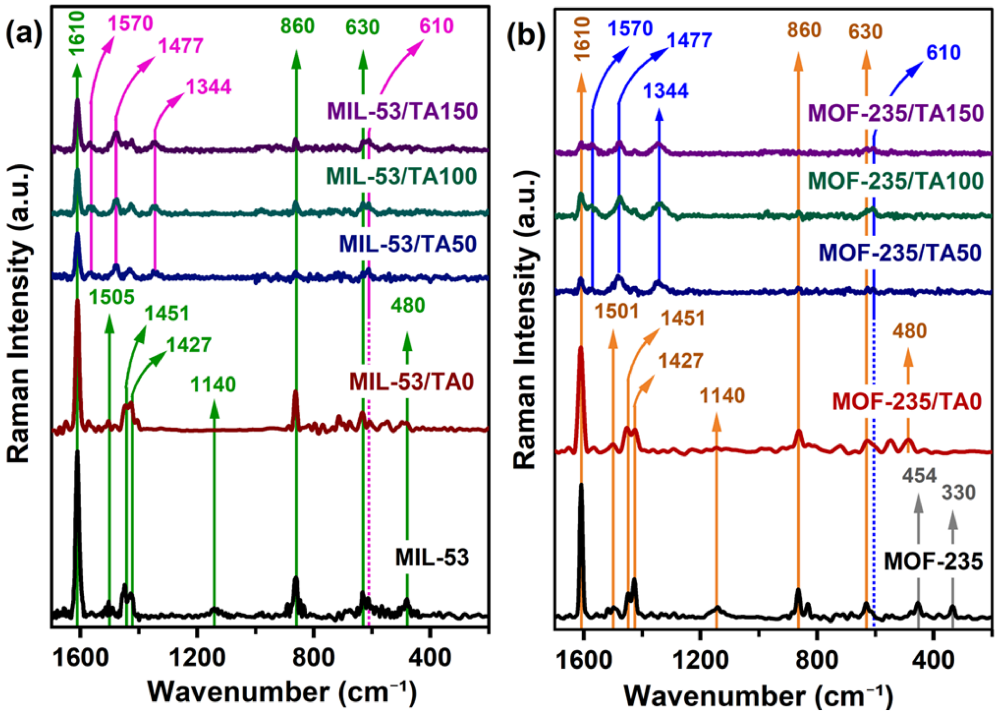

Figure 4. Raman spectra of (**a**) MIL-53 and (**b**) MOF-235, water-treated and PSM with tannic acid.

Following PSM of MOF-235 with TA, the successful formation of the TA–Fe coordination complex was verified by the appearance of the characteristic bands at 1477, 1344 and 610 cm^{-1} (indicated by blue arrows in Figure 4b), matching the profiles observed in the PSM of MIL-53 samples. However, a noticeable change in the intensity of the peak at 1610 cm^{-1} was observed in the MOF-235/TAx series. As discussed, hydrolysis of the MOF-235 released free Fe^{3+} ions into solution. In the presence of tannic acid, these leached Fe^{3+} ions co-assemble with polyphenol molecules to form an amorphous metal–phenolic network (MPN) shell, which may encapsulate the surviving MIL-53 core particle. MPNs formed by Fe-TA are structurally different from the crystalline coordination nodes of the MOF. Therefore, electronic interactions between Fe^{3+}-BDC in the MOF structure and the free Fe^{3+} ions coordinated with TA within the MPNs could alter the overall electronic delocalization and polarizability across the aromatic systems. Consequently, these electronic modifications altered the vibrational dynamics of the materials, inducing peak broadening in the Raman spectra.

Powder X-ray diffraction (XRD) was performed to evaluate the phase transitions, structural flexibility, and long-range crystalline integrity of the frameworks before and after PSM with TA. According to the XRD patterns of the MIL-53 series (Figure 5a), the PVP-modulated MIL-53 exhibited well-defined diffraction peaks at 9.4°, 11.3° and 18.7°, closely matching the reference pattern (Rietveld plot II) of the MIL-53(Fe) crystalline phase (CIF:258445) [32,64]. However, MIL-53/TA0 exhibited a notable increase in the relative intensity of the peaks at $2\theta \approx 11°$ and 17.6°, along with the appearance of a new peak at ≈28°. The differences between MIL-53 and MIL-53/TA0 diffraction patterns reflected a crystal phase transition toward the narrow-pore crystal form of MIL-53, which is associated with a

smaller unit cell volume (Figure 5a Rietveld plot III), attributed to the well-known breathing effect of the flexible MIL-53 framework [65]. This crystal phase transition in MIL-53 is due to host-guest or guest-guest interactions, where the presence of water molecules inside the pores can be regarded as a guest molecule [66,67]. Water treatment in MIL-53 first purified the pores by removing residual or trapped unreacted materials. Subsequently, this purification process allowed water molecules (as a guest) to enter the pores, where the hydrogen atoms of water interacted strongly with the oxygen groups of the chains, leading to volume shrinkage and the crystal phase transition to the narrow-pore form, which is almost similar to the MIL-53(Fe)[H_2O] phase [65,68,69].

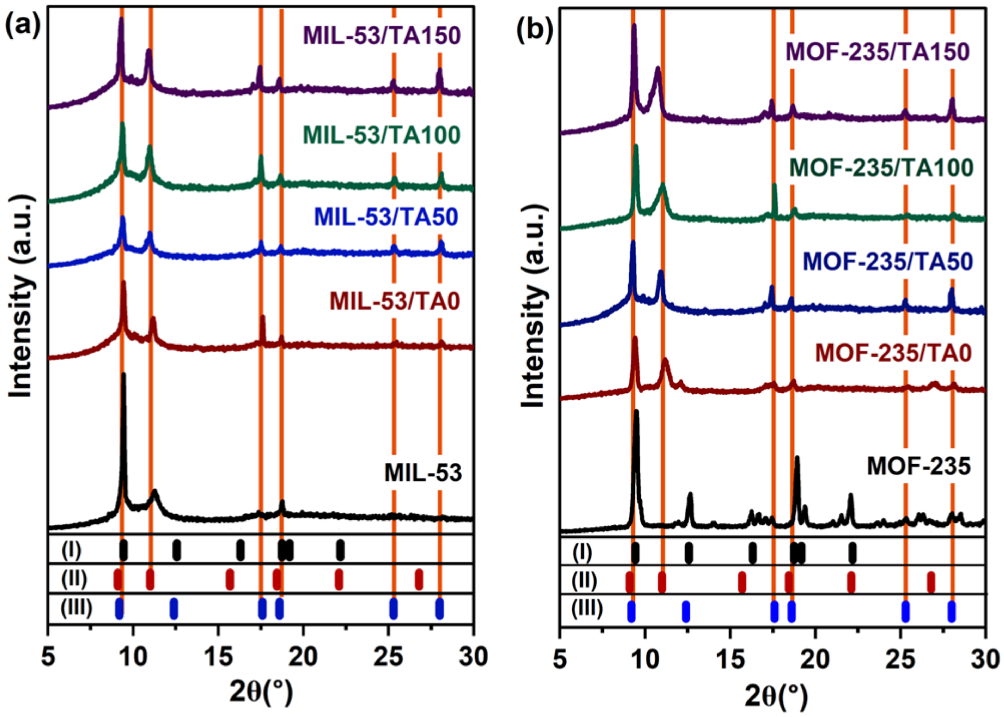

Figure 5. XRD patterns of (**a**) MIL-53 and (**b**) MOF-235, water-treated and PSM with different amounts of tannic acid. The final Rietveld plots (I) MOF-235, (II) Fe(BDC)(DMF), (III) MIL-53(Fe)[H_2O] were calculated from CIF files [32,64,65]. The orange vertical lines highlight the characteristic diffraction peaks corresponding to the final Rietveld plots.

Regarding the TA-modified series of MIL-53, the topology of MIL-53 was fully preserved following TA incorporation, compared to MIL-53/TA0 (Figure 5a). This observation was consistent with the FTIR results, where the characteristic bands of MIL-53 remained largely unchanged, except for variations associated with hydroxyl groups upon TA incorporation [56]. Interestingly, PSM with the lowest TA concentration (MIL-53/TA50) reduced overall diffraction peak intensity, attributed to the inherently amorphous nature of TA, causing localized, disordered surface adsorption. However, the intensity of the diffraction peaks in MIL-53/TA100 and MIL-53/TA150 almost recovered. This intensity recovery suggested that higher TA concentrations provided a sufficient chemical potential gradient to drive polyphenol molecules deeper into the porous channel network, establishing ordered host–guest interactions. This finding aligns well with physisorption results of the MIL-53/TAx series.

The XRD pattern of the MOF-235 series is presented in Figure 5b. Characteristic peaks of sonochemically synthesized MOF-235 at 2θ = 9.4° (101), 12.6° (102), 16.2° (200), 18.8° (202), 19.3° (004), and 22° (3–11) matched the reference of MOF-235 (CIF:255079) [32]. However, after dispersing MOF-235 in deionized water for 1 h followed by drying, the XRD

pattern of MOF-235/TA0 underwent significant structural changes compared to MOF-235, consistent with the trends observed in FTIR, Raman and SEM images. Several characteristic peaks of MOF-235/TA0 sample such as 12.6°, 16.2°, 19.3° and 22° disappeared, while new peaks at 2θ ≈ 11.2°, 12°, 27° and 28.2° appeared. These newly formed peaks closely matched the diffraction pattern of MIL-53 [64,70]. This observation is also consistent with the FTIR result of MOF-235/TA0, where the asymmetric band shifted and the structure gradually became more similar to MIL-53. The XRD patterns of the PSM of the MOF-235 series in Figure 5b demonstrated that the overall framework topology remained largely intact compared to that of MOF-235/TA0. However, slight variations in the peak around 2θ ≈ 11° were observed, which could be attributed to the breathing behavior of the remaining MIL-53 framework, as well as guest–host interactions with TA molecules adsorbed on the external crystal surface or within the accessible pore channels, consistent with the trends observed for the PSM of MIL-53 (Figure 5a) [56,70].

3.3. Thermal Stability and Compositional Analysis

The thermal stability and relative framework compositions were evaluated by thermogravimetric analysis (TGA) for both the MIL-53 and MOF-235 series under N_2 atmosphere (Figure 6).

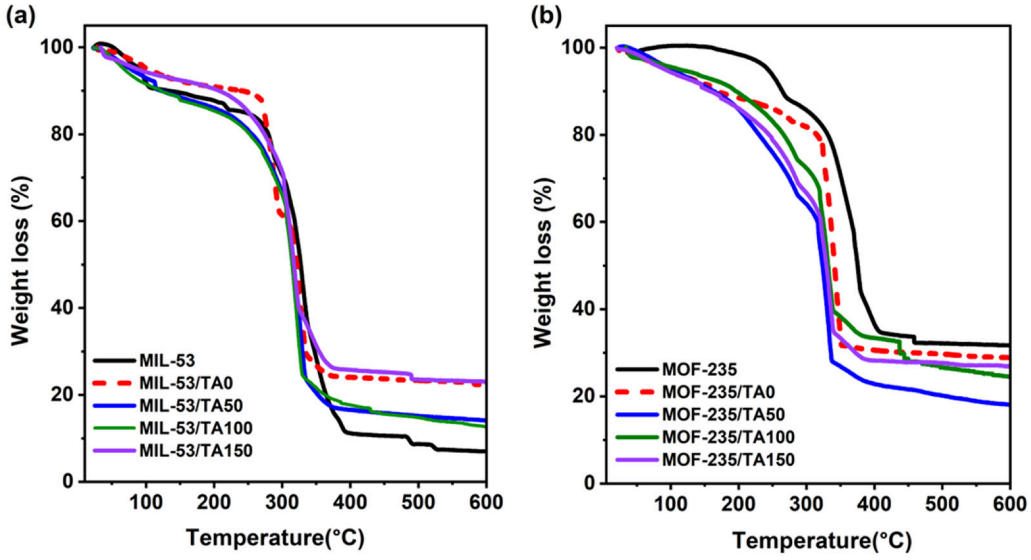

Figure 6. TGA curves of (**a**) MIL-53 and (**b**) MOF-235, water-treated and PSM with tannic acid.

The thermal decomposition of the MIL-53 series (Figure 6) generally occurred in two main steps, reflecting the stability of the crystal structure. The gradual weight loss below 270 °C corresponded to the evaporation of water molecules and residuals trapped within the porous channels. A sharp, rapid weight loss was observed between 300 and 400 °C, representing the decomposition of the organic (BDC) linkers and the PVP modulator, and the subsequent collapse of the MOF framework and final inorganic part, which is composed of iron oxide [65,69]. Conversely, the thermal decomposition of the MIL-53/TA0 (red dashed curve, Figure 6a) displayed slightly lower temperature weight loss compared to MIL-53, reflecting the effect of purification and crystal phase changes to a narrow-pore phase, as discussed in the XRD results [65,69]. Following PSM of MIL-53, the TGA results of MIL-53/TAx show very similar curves, indicating that TA incorporation mainly affected guest–framework interactions rather than the fundamental framework stability. Alternatively, the TGA pattern of MOF-235 (Figure 6b) showed that the initial weight loss below 350 °C corresponded to the loss of excess solvent, residual and 3-ligated DMF molecules and rapid

framework collapse after 350 °C, representing the MOF-235 framework decomposition [32]. The TGA profile of MOF-235/TA0 demonstrated a decomposition around 300–320 °C, almost identical to that of MIL-53/TA0. This thermal signature provided definitive thermodynamic proof of the structural instability of MOF-235 in aqueous media due to counter-anion dissociation and framework collapse, whereas thermodynamically stable MIL-53 remained intact, as supported by the other characterization results in this work. In the case of the MOF-235/TAx series, the TGA curves exhibited a more gradual, sloped weight loss below ≈330 °C. Wang et al. reported that the thermal decomposition of Fe–TA complexes occurs between 100 and 330 °C [71]. Therefore, this sloped weight loss below ≈330 °C in the MOF-235/TAx series can be attributed to the preliminary thermal decomposition of the Fe–polyphenol (Fe-TA) complexes before the structural collapse of the remaining MIL-53 framework.

3.4. UV-Vis Absorption Properties

To further investigate the UV-vis absorption properties and photo-response of the MOFs before and after PSM with TA, UV-visible diffuse reflectance spectroscopy (DRS) was performed. A comparison of the water-treated MOFs (TA0) and their corresponding maximum amount of TA (TA150) is presented in Figure 7, while the complete series is provided in the Supplementary Materials (Figure S3).

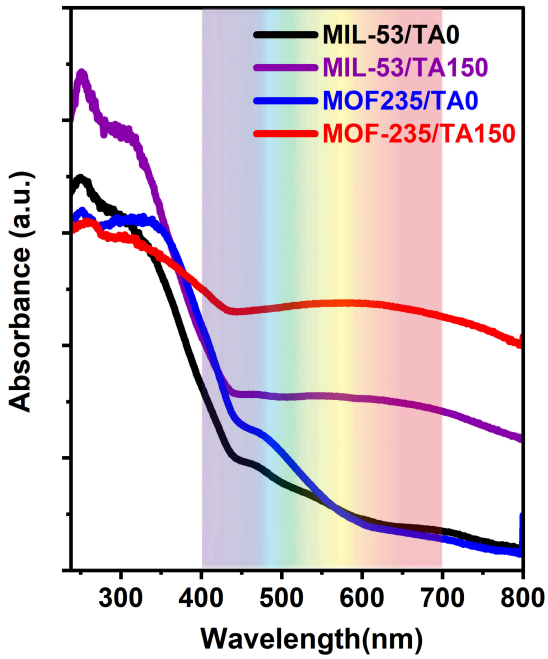

Figure 7. UV–vis DRS spectra of water-treated (TA0) and TA150-modified MIL-53 and MOF-235.

According to the UV-vis spectra of all samples, the peak at 250 nm is assigned to oxygen-to-Fe^{3+}, ligand-to-metal charge transfer (LMCT), and a weak peak at 460 nm corresponds to the spin-forbidden d-d transition [17,72]. Following PSM of MOFs with TA, a new broad absorption band across the visible and near-infrared (visible-NIR) region (500 to 800 nm) could be observed. This new absorption feature can be attributed to the formation of iron-polyphenol complexes. The coordination between the metal and the hydroxyl group of TA facilitates ligand-to-metal charge transfer (LMCT), thereby enhancing light absorption in the visible-NIR region. Accordingly, MIL-53/TA150 and MOF-235/TA150 exhibited the highest visible-light absorption, consistent with their higher TA content. Notably, according to Figure 7, the UV-vis results of MOF-235/TA150 (red curve) displayed a higher optical absorption intensity compared to MIL-53/TA150 (purple curve) in the range from 500 to

800 nm. This enhanced absorbance of MOF-235/TA150 is driven by a thick surface MPN layer (supporting the physisorption, Raman and FTIR, and TGA findings), which resulted in a higher surface density of Fe-TA complex and enhanced LMCT, consequently higher visible–NIR optical absorption compared to MIL-53/TA150. Overall, the enhanced visible-light absorption of both Fe-based MOFs following PSM with TA improves their visible-light responsiveness. This enhanced visible-light absorption highlights their potential not only in photothermal applications but also in diverse visible-light-driven applications, such as solar-driven water splitting, carbon dioxide (CO_2) reduction, wastewater decontamination, biomedical and optoelectronic sensing [73–75].

3.5. Photothermal Performance

To investigate the light-to-heat conversion performance of MIL-53 and MOF-235, photothermal conversion experiments were conducted under dry state conditions. According to the UV-vis diffuse reflectance spectra, the water-treated MOFs exhibited weak light absorption in the visible region, resulting in relatively low photothermal effects. However, PSM of MOFs with tannic acid enhanced light absorption in the visible-NIR region, which could improve the light-to-heat conversion of MOFs.

Based on the optical absorbance of MOFs, MIL-53/TA150 and MOF-235/TA150 were selected to evaluate the capability of photothermal conversion and compared directly with MIL-53/TA0 and MOF-235/TA0. The surface temperature evolution of all MOF samples alongside the baseline control is illustrated in Figure 8a, while corresponding thermal images captured by an infrared (IR) camera are presented in Figure S4. Upon continuous visible-light irradiation (632.5 nm) for 10 min, the baseline control showed only a minimal temperature increase (rising from 21 °C to 22 °C), confirming that ambient or laser background heating was negligible. In contrast, MOF-235/TA0 displayed a moderate surface temperature increase to ≈31 °C ($\Delta T \approx 6$ °C, where $\Delta T = T_{max} - T_0$), while the surface temperature of MOF-235/TA150 reached ≈37 °C ($\Delta T \approx 14$ °C). The photothermal test of MIL-53/TA0 reached a surface temperature of ≈36 °C ($\Delta T \approx 10$ °C), whereas MIL-53/TA150 exhibited the most noticeable photothermal response, reaching 47 °C ($\Delta T \approx 25$ °C). Interestingly, despite MOF-235/TA150 displaying higher absorption in the visible region (Figure 7), MIL-53/TA150 achieved a significantly higher photothermal temperature rise (Figure 8a). This unexpected behavior arises from key morphological and structural differences between the two systems.

While previous literature reported that conventional MIL-53(Fe) exhibits negligible photothermal conversion [53], MIL-53/TA0 demonstrated an inherent light-to-heat conversion capability ($\Delta T \approx 10$ °C). This property was directly influenced by the tailored physicochemical characteristics achieved through our synthesis strategy [54,76]. In contrast to conventional (solvothermal) synthesis methods requiring harsh temperatures and long reaction times (e.g., more than one week at 120 °C or 2 days at 150 °C), our PVP-modulated sonochemical route not only rapidly yielded crystalline MIL-53(Fe) (6 h at 70 °C), but also promoted particle size uniformity, superior spatial dispersity, and enhanced textural properties. This uniform morphology induced localized optical scattering and light-trapping effects within the powder bed, thereby improving photon absorption and non-radiative vibrational relaxation. Furthermore, previous studies reported photothermal properties of TA-modified MIL-53 under NIR irradiation, whereas in this work the photothermal response of MIL-53/TA150 was achieved under a visible laser at 632.5 nm. This exceptional photothermal performance of MIL-53/TA150 was enabled by the enhanced specific surface area and higher density of accessible active iron centers in our sonochemically synthesized MIL-53 particles, which facilitated extensive TA coordination during PSM.

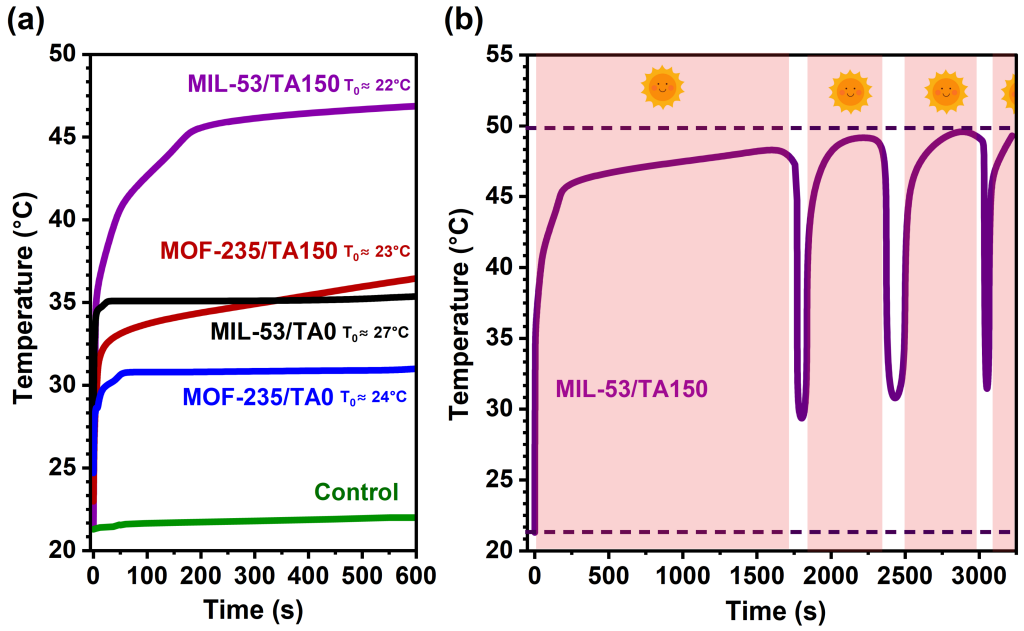

Figure 8. (**a**) Temperature rise curves of water-treated (TA0) and TA150-modified MIL-53 and MOF-235 in the dry state under 632.5 nm irradiation for 600 s (T_0 indicates the starting temperature). (**b**) Photothermal switching response of MIL-53/TA150 over three light on–off cycles (shaded red areas indicate laser-on periods).

On the other hand, although photothermal conversion of MOF-235 has never been previously investigated, sonochemically synthesized MOF-235 (6 h at 70 °C) along with PSM with TA demonstrated visible light photothermal performance. While the structural instability of MOF-235 in aqueous environments conventionally presents a major limitation for classical PSM, a one-pot water-induced dissolution-construction process was employed to overcome this limitation. Characterization techniques in this work, particularly Raman and FTIR spectroscopy, provided evidence of water-induced hydrolysis, $[FeCl_4]^-$ anion leaching and iron-polyphenol electronic interaction. The localized leaching of Fe^{3+} ions in the presence of tannic acid promoted the in situ self-assembly of photothermally active metal–phenolic networks (MPNs) alongside the durable MIL-53 framework. Ultimately, this process converted a hydrolytically unstable precursor into an effective photothermal material, achieving a maximum surface temperature of ≈37 °C for MOF-235/TA150.

Based on the higher temperature rise observed for MIL-53/TA150, the light-to-heat conversion efficiency, photothermal stability, durability, and sensitivity of this sample were investigated. The light-to-heat conversion efficiency, calculated via an energy balance model that accounts for the incident laser power, the temperature-rise kinetics within the first 5 s, and a specific heat capacity, calculated from TGA/DSC analysis, Cp = 1.41 J/g K, was as high as ≈46% under visible laser irradiation (632.5 nm). To assess long-term stability, the sample was subjected to continuous laser irradiation for 40 min. As presented in Figure 8b, the surface temperature remained extremely stable around ≈47 °C without any noticeable thermal decay, indicating the chemical and structural robustness of the MOF under prolonged optical stress. Subsequently, the transient thermal sensitivity was investigated by performing three consecutive light on–off cycles consisting of a 1 min cooling period (laser off) followed by a 2 min heating period (laser on). MIL-53/TA150 demonstrated a reproducible response, cooling toward ambient temperature when the light was off and returning to its maximum equilibrium temperature of ≈47 °C during light-on periods. This reproducible square-wave-like thermal response confirmed that the MIL-53/TA150 possesses excellent sensitivity and cycle-to-cycle stability, making it

a promising candidate for cyclic photothermal energy conversion. However, additional studies are required to extend the application of these optimized photothermal materials into broader solar-driven technologies.

4. Conclusions

In this work, tannic acid (TA) was successfully integrated as a post-synthetic modification agent for sonochemically synthesized MOF-235(Fe) and PVP-modulated MIL-53(Fe), tailoring their framework dynamics and visible-light photothermal properties. A comprehensive suite of characterization techniques (XRD, N_2 physisorption, TGA, FTIR, Raman, and DRS) was combined with photothermal testing to systematically explain the structure–property relationships governing these iron–polyphenol MOF composites. FTIR and Raman spectroscopy provided evidence of chemical coordination between Fe and TA. This intense Fe–polyphenol chelation significantly tuned the optical absorption profiles, yielding broad absorbance across the visible and near-infrared regions and facilitating ligand-to-metal charge transfer (LMCT).

Notably, this work presented the first report on engineering the photothermal properties of MOF-235 by overcoming the framework instability via controlled dissolution–construction. While MOF-235 conventionally suffered from structural collapse in aqueous media, a one-pot water-induced dissolution–construction mechanism was established to transform the limitation of MOF-235 into a synthetic tool. Spectroscopic analysis confirmed that aqueous dispersion induced $[FeCl_4]^-$ leaching (evidenced by the complete disappearance of the characteristic 330 cm^{-1} Raman peak) and the selective hydrolysis of the unstable MOF-235 phase. The released Fe^{3+} ions self-assembled with TA into photothermally active metal–phenolic network (MPN) shells around the surviving, thermodynamically stable MIL-53 core, elevating the equilibrium surface temperature of MOF-235/TA150 to ≈37 °C.

For the MIL-53 series, PVP-modulated sonochemical synthesis yielded uniform nanoscale morphology that promoted light trapping and optical scattering. Consequently, MIL-53/TA150 achieved a maximum surface temperature of ≈47 °C and a remarkable light-to-heat conversion efficiency of ≈46% under 632.5 nm visible laser irradiation. MIL-53/TA150 demonstrated outstanding thermal stability during 40 min of continuous illumination and excellent cycling durability across repeated light on–off cycles. Overall, this work demonstrated that PSM with TA can overcome the intrinsic limitations of iron-based MOFs by tailoring their structural dynamics and boosting visible-light-to-heat conversion (632.5 nm), thereby providing a promising strategy for green thermal energy generation.

Supplementary Materials: The following supporting information can be downloaded at https://www.mdpi.com/article/10.3390/chemistry8120167/s1: Figure S1: SEM images of (a) MIL-53 and (b) MOF-235, water-treated and PSM with different amounts of tannic acid; Figure S2: (a) The BJH pore size distribution and (b) nitrogen adsorption–desorption isotherms of MIL-53, water-treated and PSM with different amounts of tannic acid. (c) The BJH pore size distribution and (d) nitrogen adsorption–desorption isotherms of MOF-235, water-treated and PSM with different amounts of tannic acid; Figure S3: UV–vis DRS spectra of (a) MIL-53, (b) MOF-235, water-treated, and PSM with different amounts of tannic acid; Figure S4: Infrared (IR) thermal images of MIL-53/TA150 recorded under 632.5 nm visible-light laser irradiation at different time intervals (t, in seconds). The solid black rectangles indicate the laser-irradiated sample regions, where the surface temperature was measured, while the dashed black circles indicate the ambient background reference regions, which were not directly exposed to laser irradiation and were used to monitor the background temperature; Table S1: Textural Properties of MOFs, water-treated and PSM with different amounts of tannic acid; Table S2. The optical bandgap values of MIL-53 and MOF-235, water-treated, and PSM with different amounts of tannic acid.

Author Contributions: Conceptualization, F.S. and A.M.-C.; Methodology, F.S. and A.M.-C.; Validation, F.S. and A.M.-C.; Formal analysis, F.S. and A.M.-C.; Investigation, F.S. and A.M.-C.; Data curation, F.S.; Writing—original draft, F.S. and A.M.-C.; Writing—review & editing, F.S. and A.M.-C.; Visualization, F.S. and A.M.-C.; Supervision, A.M.-C.; Project administration, F.S. and A.M.-C.; Funding acquisition, A.M.-C. All the authors contributed equally. All authors have read and agreed to the published version of the manuscript.

Funding: This research was funded by Secretaría de Ciencia, Humanidades, Tecnología e Innovación (SECIHTI) from Mexico for the financial support (grant no. 2022-000002-01NACF-03589).

Data Availability Statement: The original contributions presented in this study are included in the article/Supplementary Materials. Further inquiries can be directed to the corresponding author.

Acknowledgments: Grammatical errors were checked and corrected using Grammarly (V1.2.310.2001) and Gemini Notebook (Version 1.67.7). The text was critically verified and revised by the authors, who take full responsibility for the final manuscript.

Conflicts of Interest: The authors declare no conflicts of interest.

Abbreviations

The following abbreviations are used in this manuscript:

TA	Tannic Acid
BDC	Terephthalic Acid
MOFs	Metal–Organic Frameworks
MPNs	Metal–Phenolic Networks
MIL	Materials of Institute Lavoisier
PSM	Post-Synthetic Modification
PVP	Polyvinylpyrrolidone
LMCT	Ligand-to-Metal Charge Transfer
Cp	Specific Heat Capacity

References

1. Climate Change. Available online: https://www.who.int/health-topics/climate-change#tab=tab_1 (accessed on 22 September 2025).
2. Solomon, S.; Plattner, G.K.; Knutti, R.; Friedlingstein, P. Irreversible Climate Change Due to Carbon Dioxide Emissions. *Proc. Natl. Acad. Sci. USA* **2009**, *106*, 1704–1709. [CrossRef] [PubMed]
3. Baklouti, I.; Mujeebu, M.A.; Noor, M.M. Next-Generation Renewable Thermal Systems: A Roadmap for Integration, Intelligence, and Decarbonization. *Appl. Therm. Eng.* **2026**, *295*, 130618. [CrossRef]
4. Renewable Heat—Renewables 2025—Analysis—IEA. Available online: https://www.iea.org/reports/renewables-2025/renewable-heat (accessed on 24 August 2026).
5. Ambient (Outdoor) Air Pollution. Available online: https://www.who.int/news-room/fact-sheets/detail/ambient-(outdoor)-air-quality-and-health (accessed on 22 September 2025).
6. Pozzer, A.; Steffens, B.; Proestos, Y.; Sciare, J.; Akritidis, D.; Chowdhury, S.; Burkart, K.; Bacer, S. Atmospheric Health Burden across the Century and the Accelerating Impact of Temperature Compared to Pollution. *Nat. Commun.* **2024**, *15*, 9379. [CrossRef] [PubMed]
7. Cui, X.; Ruan, Q.; Zhuo, X.; Xia, X.; Hu, J.; Fu, R.; Li, Y.; Wang, J.; Xu, H. Photothermal: A Powerful Light-to-Heat. *Chem. Rev.* **2023**, *123*, 6891–6952. [CrossRef] [PubMed]
8. Dias, L.F.G.; Abou-Hassan, A. Different Applications, Same Story: Inspiring Nanomedicine from Photothermal Catalysis to Modulate the Photothermal Activity of Nanomaterials through Defects Engineering. *Coord. Chem. Rev.* **2024**, *507*, 215751. [CrossRef]
9. Guo, Z.; Xiao, Y.; Wu, W.; Zhe, M.; Yu, P.; Shakya, S.; Li, Z.; Xing, F. Metal–Organic Framework-Based Smart Stimuli-Responsive Drug Delivery Systems for Cancer Therapy: Advances, Challenges, and Future Perspectives. *J. Nanobiotechnology* **2025**, *23*, 157. [CrossRef] [PubMed]
10. Yu, X.; Fan, S.; Zhu, B.; El-Hout, S.I.; Zhang, J.; Chen, C. Recent Progress on Photothermal Nanomaterials: Design, Mechanism, and Applications. *Green Energy Environ.* **2025**, *10*, 1377–1436. [CrossRef]

11. Mukherjee, A.; Okolie, J.A.; Abdelrasoul, A.; Niu, C.; Dalai, A.K. Review of Post-Combustion Carbon Dioxide Capture Technologies Using Activated Carbon. *J. Environ. Sci.* **2019**, *83*, 46–63. [CrossRef] [PubMed]
12. Ganiyu, S.A. Review of Zeolitic-Based Sorbents for CO_2 Capture: Insights into Functional Modifications, Economic Feasibility and Machine Learning-Enhanced Strategies. *Chem. Eng. J. Adv.* **2025**, *23*, 100818. [CrossRef]
13. Samanidou, V.F.; Deliyanni, E.A. Metal Organic Frameworks: Synthesis and Application. *Molecules* **2020**, *25*, 960. [CrossRef] [PubMed]
14. Song, Y.; Ma, S. Pore Engineering in Metal–Organic Frameworks and Covalent Organic Frameworks: Strategies and Applications. *Chem. Sci.* **2025**, *16*, 11740–11767. [CrossRef] [PubMed]
15. Xie, Z.; Hou, J. Industrialising Metal–Organic Frameworks—Bridging Laboratory Innovation and Future Applications. *Ind. Eng. Chem. Res.* **2025**, *64*, 7941–7955. [CrossRef]
16. Hui, Q.; Fu, J.; Xu, H.; Wang, C.; Ding, Q.; Zhu, W.; Sun, J.; Zhou, Z.; Wu, Y.; Hu, X.; et al. Metal–Organic Frameworks for CO_2 Capture: Challenges and Efforts from Laboratory Research to Industrial Applications. *Ind. Eng. Chem. Res.* **2025**, *64*, 9457–9483. [CrossRef]
17. Chen, H.; Liu, Y.; Cai, T.; Dong, W.; Tang, L.; Xia, X.; Wang, L.; Li, T. Boosting Photocatalytic Performance in Mixed-Valence MIL-53(Fe) by Changing FeII/FeIII Ratio. *ACS Appl. Mater. Interfaces* **2019**, *11*, 28791–28800. [CrossRef] [PubMed]
18. Khan, I.S.; Garzon-Tovar, L.; Mateo, D.; Gascon, J. Metal-Organic-Frameworks and Their Derived Materials in Photo-Thermal Catalysis. *Eur. J. Inorg. Chem.* **2022**, *2022*, e202200316. [CrossRef]
19. May, A.M.; Dempsey, J.L. A New Era of LMCT: Leveraging Ligand-to-Metal Charge Transfer Excited States for Photochemical Reactions. *Chem. Sci.* **2024**, *15*, 6661–6678. [CrossRef] [PubMed]
20. Arjmandi, M.; Khayet, M.; Horcajada, P. A Holistic Review of MOF-Based Solar-Driven Atmospheric Water Harvesting. *Prog. Mater. Sci.* **2026**, *158*, 101648. [CrossRef]
21. El-Morsy, M.T.; Elshekh, A.; Ghazy, M.E.S.; Askar, N.M.; Ali, M.M.; Shams, G.; Essam, A.; Khafaga, D.S.R.; Fahmy, S.A.; Babker, A. Metal–Organic Framework-Based Therapeutic Strategies for Hepatocellular Carcinoma: Current Advances and Future Perspectives. *Cancer Nanotechnol.* **2026**, *17*, 43. [CrossRef]
22. Ji, S.; Zhang, J.; Su, G.; Dang, L.; Wang, Z. PCN-224@ZIF-8 Core-Shell Heterojunctions Synergistic Photocatalytic and Photothermal Effects for Antibacterial and Wound Healing Applications. *J. Colloid Interface Sci.* **2025**, *696*, 137864. [CrossRef] [PubMed]
23. Espín, J.; Garzón-Tovar, L.; Carné-Sánchez, A.; Imaz, I.; Maspoch, D. Photothermal Activation of Metal-Organic Frameworks Using a UV-Vis Light Source. *ACS Appl. Mater. Interfaces* **2018**, *10*, 9555–9562. [CrossRef] [PubMed]
24. Reddy Velagala, S.K.; Sabri, Y.; Parthasarathy, R.; Sreedhar, I. A Bird's Eye View of Recent Advances in Direct Air Capture of CO_2 Using MOFs. *Fuel* **2026**, *405*, 136525. [CrossRef]
25. Asad, Z.; Zeeshan, M.; Khan, M.Y.; Shahid, M. Emerging Trends in N-Based Metal–Organic Frameworks (MOFs) for CO_2 Sequestration and Catalytic Conversion into Value-Added Products: An Integrated Strategy for Clean Energy Solutions. *Coord. Chem. Rev.* **2026**, *548*, 217190. [CrossRef]
26. Ruan, Y.; Kong, L.; Zhong, Y.; Diao, Z.; Shih, K.; Hou, L.; Wang, S.; Chen, D. Review on the Synthesis and Activity of Iron-Based Catalyst in Catalytic Oxidation of Refractory Organic Pollutants in Wastewater. *J. Clean. Prod.* **2021**, *321*, 128924. [CrossRef]
27. Liu, X.; Liang, T.; Zhang, R.; Ding, Q.; Wu, S.; Li, C.; Lin, Y.; Ye, Y.; Zhong, Z.; Zhou, M. Iron-Based–Organic Frameworks in Drug and Biomedicine. *ACS Appl. Mater. Interfaces* **2021**, *13*, 9643–9655. [CrossRef] [PubMed]
28. Yu, Z.; Lepoitevin, M.; Serre, C. Iron-MOFs for Biomedical Applications. *Adv. Healthc. Mater.* **2025**, *14*, 2402630. [CrossRef] [PubMed]
29. Achenbach, B.; Yurdusen, A.; Stock, N.; Maurin, G.; Serre, C. Synthetic Aspects and Characterization Needs in MOF Chemistry—From Discovery to Applications. *Adv. Mater.* **2025**, *37*, 2411359. [CrossRef] [PubMed]
30. Dong, J.; Li, T.; Yan, H.; Chen, Y.; Wang, C.; Luan, X.; Li, X.; Li, H.; Du, X. Smart Iron-Based Metal–Organic Framework Nanovehicles Gated with CuII-Tannic Acid Coordination Polymers for Combination Therapy of Chemotherapy and Chemodynamic Therapy. *Colloids Surf. A Physicochem. Eng. Asp.* **2024**, *683*, 133101. [CrossRef]
31. Camargo, L.P.; da Silva, P.R.C.; Batagin-Neto, A.; Klobukoski, V.; Vidotti, M.; Dall'Antonia, L.H. Over 21.0% Faradaic Efficiency of Ambient Ammonia Production: Photoelectrocatalytic Activity of MOF-235. *Appl. Mater. Today* **2022**, *28*, 101540. [CrossRef]
32. Sudik, A.C.; Côté, A.P.; Yaghi, O.M. Metal-Organic Frameworks Based on Trigonal Prismatic Building Blocks and the New "Acs" Topology. *Inorg. Chem.* **2005**, *44*, 2998–3000. [CrossRef] [PubMed]
33. Liu, K.; Chen, Y.; Dong, X.; Huang, H. Simultaneous Voltammetric Determination of Dopamine and Uric Acid Based on MOF-235 Nanocomposite. *Inorg. Chem. Commun.* **2022**, *142*, 109584. [CrossRef]
34. Beltrán-Suito, R.; Pinedo-Flores, A.; Bravo-Hualpa, F.; Ramos-Muñoz, J.; del Rosario Sun-Kou, M. Adsorption of N,N-Dimethylamine from Aqueous Solutions by a Metal Organic Framework, MOF–235. *J. Dispers. Sci. Technol.* **2019**, *40*, 901–908. [CrossRef]
35. Lata, S.; Ansari, N.G. Iron-Based Metal–Organic Frameworks as Efficient Adsorbents for Wastewater Remediation: Insight into Mechanistic, Ecotoxicological and Disposal Concerns. *Microporous Mesoporous Mater.* **2026**, *402*, 113945. [CrossRef]

36. Millange, F.; Walton, R.I. MIL-53 and Its Isoreticular Analogues: A Review of the Chemistry and Structure of a Prototypical Flexible Metal-Organic Framework. *Isr. J. Chem.* **2018**, *58*, 1019–1035. [CrossRef]
37. Férey, G.; Serre, C. Large Breathing Effects in Three-Dimensional Porous Hybrid Matter: Facts, Analyses, Rules and Consequences. *Chem. Soc. Rev.* **2009**, *38*, 1380–1399. [CrossRef] [PubMed]
38. Ling, S.; Slater, B. Unusually Large Band Gap Changes in Breathing Metal-Organic Framework Materials. *J. Phys. Chem. C* **2015**, *119*, 16667–16677. [CrossRef]
39. Figueroa-Quintero, L.; Villalgordo-Hernández, D.; Delgado-Marín, J.J.; Narciso, J.; Kumar Velisoju, V.; Castaño, P.; Gascón, J.; Ramos-Fernández, E. V Post-Synthetic Surface Modification of Metal–Organic Frameworks and Their Potential Applications. *Small Methods* **2023**, *7*, 2201413. [CrossRef] [PubMed]
40. Ding, M.; Flaig, R.W.; Jiang, H.L.; Yaghi, O.M. Carbon Capture and Conversion Using Metal–Organic Frameworks and MOF-Based Materials. *Chem. Soc. Rev.* **2019**, *48*, 2783–2828. [CrossRef] [PubMed]
41. Ji, Z.; Wang, H.; Canossa, S.; Wuttke, S.; Yaghi, O.M. Pore Chemistry of Metal–Organic Frameworks. *Adv. Funct. Mater.* **2020**, *30*, 2000238. [CrossRef]
42. Markopoulou, P.; Forgan, R.S. Chapter 12—Postsynthetic Modification of MOFs for Biomedical Applications. In *Metal-Organic Frameworks for Biomedical Applications*; Mozafari, M., Ed.; Woodhead Publishing: Cambridge, UK, 2020; pp. 245–276. ISBN 978-0-12-816984-1.
43. Bose, S.; Sengupta, D.; Rayder, T.M.; Wang, X.; Kirlikovali, K.O.; Sekizkardes, A.K.; Islamoglu, T.; Farha, O.K. Challenges and Opportunities: Metal–Organic Frameworks for Direct Air Capture. *Adv. Funct. Mater.* **2024**, *34*, 2307478. [CrossRef]
44. Lee, G.; Hossain, M.A.; Yoon, M.; Jhung, S.H. Nanoarchitectonics of Metal–Organic Frameworks Having Hydroxy Group for Adsorption, Catalysis, and Sensing. *J. Ind. Eng. Chem.* **2023**, *119*, 181–192. [CrossRef]
45. Khanbabaee, K.; van Ree, T. Tannins: Classification and Definition. *Nat. Prod. Rep.* **2001**, *18*, 641–649. [CrossRef] [PubMed]
46. Molino, S.; Pilar Francino, M.; Ángel Rufián Henares, J. Why Is It Important to Understand the Nature and Chemistry of Tannins to Exploit Their Potential as Nutraceuticals? *Food Res. Int.* **2023**, *173*, 113329. [CrossRef] [PubMed]
47. Guo, J.; Ping, Y.; Ejima, H.; Alt, K.; Meissner, M.; Richardson, J.J.; Yan, Y.; Peter, K.; Von Elverfeldt, D.; Hagemeyer, C.E.; et al. Engineering Multifunctional Capsules through the Assembly of Metal-Phenolic Networks. *Angew. Chem. Int. Ed.* **2014**, *53*, 5546–5551. [CrossRef] [PubMed]
48. Guo, Z.; Xie, W.; Lu, J.; Guo, X.; Xu, J.; Xu, W.; Chi, Y.; Takuya, N.; Wu, H.; Zhao, L. Tannic Acid-Based Metal Phenolic Networks for Bio-Applications: A Review. *J. Mater. Chem. B* **2021**, *9*, 4098–4110. [CrossRef] [PubMed]
49. Koopmann, A.K.; Schuster, C.; Torres-Rodríguez, J.; Kain, S.; Pertl-Obermeyer, H.; Petutschnigg, A.; Hüsing, N. Tannin-Based Hybrid Materials and Their Applications: A Review. *Molecules* **2020**, *25*, 4910. [CrossRef] [PubMed]
50. Guo, Y.; Sun, Q.; Wu, F.G.; Dai, Y.; Chen, X. Polyphenol-Containing Nanoparticles: Synthesis, Properties, and Therapeutic Delivery. *Adv. Mater.* **2021**, *33*, 2007356. [CrossRef] [PubMed]
51. Zhang, W.; Roy, S.; Ezati, P.; Yang, D.P.; Rhim, J.W. Tannic Acid: A Green Crosslinker for Biopolymer-Based Food Packaging Films. *Trends Food Sci. Technol.* **2023**, *136*, 11–23. [CrossRef]
52. Espina, A.; Cañamares, M.V.; Jurašeková, Z.; Sanchez-Cortes, S. Analysis of Iron Complexes of Tannic Acid and Other Related Polyphenols as Revealed by Spectroscopic Techniques: Implications in the Identification and Characterization of Iron Gall Inks in Historical Manuscripts. *ACS Omega* **2022**, *7*, 27937–27949. [CrossRef] [PubMed]
53. Yang, J.; Wang, D.; Wang, J.; Hu, W. Corrosion Resistance and Near-Infrared Light Induced Self-Healing Behavior of Polycaprolactone Coating with MIL-53@TA on Magnesium Alloy. *Appl. Surf. Sci.* **2022**, *585*, 152729. [CrossRef]
54. Shammiry, F.; Montesinos-Castellanos, A. Sonochemical Synthesis of MOF-235 and Polyvinylpyrrolidone (PVP)-Assisted Phase Transformation to MIL-53(Fe). *Mater. Adv.* **2025**, *6*, 7958–7968. [CrossRef]
55. Yuan, H. Growth of Metal Organic Frameworks (MOFs) Layers on Functionalized Surfaces. Ph.D. Thesis, Université Paris-Saclay (ComUE), Gif-sur-Yvette, France, 2017.
56. Devic, T.; Horcajada, P.; Serre, C.; Salles, F.; Maurin, G.; Moulin, B.; Heurtaux, D.; Clet, G.; Vimont, A.; Grenéche, J.M.; et al. Functionalization in Flexible Porous Solids: Effects on the Pore Opening and the Host−Guest Interactions. *J. Am. Chem. Soc.* **2010**, *132*, 1127–1136. [CrossRef] [PubMed]
57. Bernt, S.; Guillerm, V.; Serre, C.; Stock, N. Direct Covalent Post-Synthetic Chemical Modification of Cr-MIL-101 Using Nitrating Acid. *Chem. Commun.* **2011**, *47*, 2838–2840. [CrossRef] [PubMed]
58. De Smedt, C.; Spanoghe, P.; Biswas, S.; Leus, K.; Van Der Voort, P. Comparison of Different Solid Adsorbents for the Removal of Mobile Pesticides from Aqueous Solutions. *Adsorption* **2015**, *21*, 243–254. [CrossRef]
59. Moore, S.C.; Sarazen, M.L. Stability and Kinetics of Iron-Terephthalate MOFs with Diverse Structures in Aqueous Pollutant Degradation. *AIChE J.* **2023**, *69*, e18205. [CrossRef]
60. Dong, J.; Chen, W.; Feng, J.; Liu, X.; Xu, Y.; Wang, C.; Yang, W.; Du, X. Facile, Smart, and Degradable Metal-Organic Framework Nanopesticides Gated with FeIII-Tannic Acid Networks in Response to Seven Biological and Environmental Stimuli. *ACS Appl. Mater. Interfaces* **2021**, *13*, 19507–19520. [CrossRef] [PubMed]

61. Gaikwad, A.; Kolluru, P.V. Influence of Size and H-Bonding on the Elasto-Plastic Mechanical Behavior of PVP-TA Nanofibers. *ACS Appl. Polym. Mater.* **2024**, *6*, 3105–3114. [CrossRef]
62. Sultan, M.; Youssef, A.; Baseer, R.A. Fabrication of Multifunctional ZnO@tannic Acid Nanoparticles Embedded in Chitosan and Polyvinyl Alcohol Blend Packaging Film. *Sci. Rep.* **2024**, *14*, 18533. [CrossRef] [PubMed]
63. Díaz Hidalgo, R.J.; Córdoba, R.; Nabais, P.; Silva, V.; Melo, M.J.; Pina, F.; Teixeira, N.; Freitas, V. New Insights into Iron-Gall Inks through the Use of Historically Accurate Reconstructions. *Herit. Sci.* **2018**, *6*, 63. [CrossRef]
64. Whitfield, T.R.; Wang, X.; Liu, L.; Jacobson, A.J. Metal-Organic Frameworks Based on Iron Oxide Octahedral Chains Connected by Benzenedicarboxylate Dianions. *Solid State Sci.* **2005**, *7*, 1096–1103. [CrossRef]
65. Millange, F.; Guillou, N.; Medina, M.E.; Férey, G.; Carlin-Sinclair, A.; Golden, K.M.; Walton, R.I. Selective Sorption of Organic Molecules by the Flexible Porous Hybrid Metal-Organic Framework MIL-53(Fe) Controlled by Various Host-Guest Interactions. *Chem. Mater.* **2010**, *22*, 4237–4245. [CrossRef]
66. Millange, F.; Serre, C.; Guillou, N.; Férey, G.; Walton, R.I. Structural Effects of Solvents on the Breathing of Metal–Organic Frameworks: An In Situ Diffraction Study. *Angew. Chem.* **2008**, *120*, 4168–4173. [CrossRef]
67. Ling, S.; Walton, R.I.; Slater, B. Theoretical Study of Conformational Disorder and Selective Adsorption of Small Organic Molecules in the Flexible Metal-Organic Framework Material MIL-53-Fe. *Mol. Simul.* **2015**, *41*, 1348–1356. [CrossRef]
68. Millange, F.; Guillou, N.; Walton, R.I.; Grenèche, J.M.; Margiolaki, I.; Férey, G. Effect of the Nature of the Metal on the Breathing Steps in MOFs with Dynamic Frameworks. *Chem. Commun.* **2008**, *44*, 4732–4734. [CrossRef] [PubMed]
69. Loiseau, T.; Serre, C.; Huguenard, C.; Fink, G.; Taulelle, F.; Henry, M.; Bataille, T.; Férey, G. A Rationale for the Large Breathing of the Porous Aluminum Terephthalate (MIL-53) Upon Hydration. *Chem.—A Eur. J.* **2004**, *10*, 1373–1382. [CrossRef] [PubMed]
70. Sanselme, M.; Grenèche, J.M.; Riou-Cavellec, M.; Férey, G. The First Ferric Carboxylate with a Three-Dimensional Hydrid Open-Framework (MIL-82): Its Synthesis, Structure, Magnetic Behavior and Study of Its Dehydration by Mössbauer Spectroscopy. *Solid State Sci.* **2004**, *6*, 853–858. [CrossRef]
71. Wang, C.; Li, Y.; Yuan, W.; Yang, J. A Facile Strategy for Constructing Dual Magnetic/PH-Responsive TA@Fe_3O_4 Nanocontainers Enabling Efficient Inhibitor Delivery and Enhanced Corrosion Protection. *Prog. Org. Coat.* **2026**, *214*, 110020. [CrossRef]
72. Wu, Q.; Liu, Y.; Jing, H.; Yu, H.; Lu, Y.; Huo, M.; Huo, H. Peculiar Synergetic Effect of γ-Fe_2O_3 Nanoparticles and Graphene Oxide on MIL-53 (Fe) for Boosting Photocatalysis. *Chem. Eng. J.* **2020**, *390*, 124615. [CrossRef]
73. Navalón, S.; Dhakshinamoorthy, A.; Álvaro, M.; Ferrer, B.; García, H. Metal–Organic as Photocatalysts for Solar-Driven Overall Water Splitting. *Chem. Rev.* **2023**, *123*, 445–490. [CrossRef] [PubMed]
74. Naga Prasuna, D.; Rao, A.V.; Anjani Devi, K.; Erfan, S.K.; Reddy, P.V.S.S.S.; Babu, B.V. A Review on Versatile Roles of MOFs: Bridging Biological Applications and Environmental Technologies. *Results Chem.* **2025**, *17*, 102567. [CrossRef]
75. Deng, X.; Li, Z.; García, H. Visible Light Induced Organic Transformations Using Metal-Organic-Frameworks (MOFs). *Chem.—A Eur. J.* **2017**, *23*, 11189–11209. [CrossRef] [PubMed]
76. Ehsani Nasab, M.E.; Karbasi, M.; Karbasi, M.; Varzandeh, M. Emerging Trends in MOF-Driven Photothermal Therapy: Exploring the Mechanisms and Synergistic Approaches with Photodynamic Therapy and Chemotherapy for Improved Cancer Treatment. *J. Drug Deliv. Sci. Technol.* **2025**, *114*, 107588. [CrossRef]

Disclaimer/Publisher's Note: The statements, opinions and data contained in all publications are solely those of the individual author(s) and contributor(s) and not of MDPI and/or the editor(s). MDPI and/or the editor(s) disclaim responsibility for any injury to people or property resulting from any ideas, methods, instructions or products referred to in the content.